

Strong lensing with superfluid dark matter

Sabine Hossenfelder, Tobias Mistele

*Frankfurt Institute for Advanced Studies
Ruth-Moufang-Str. 1, D-60438 Frankfurt am Main, Germany*

Abstract

In superfluid dark matter the exchange of phonons can create an additional force that has an effect similar to Modified Newtonian Dynamics (MOND). To test whether this hypothesis is compatible with observation, we study a set of strong gravitational lenses from the SLACS survey and check whether the measurements can be explained by a superfluid in the central region of galaxies.

Concretely, we try to simultaneously fit each lens's Einstein radius and velocity dispersion with a spherically symmetric density profile of a fluid that has both a normal and a superfluid component. We demonstrate that we can successfully fit all galaxies except one, and that the fits have reasonable stellar mass-to-light-ratios. We conclude that strong gravitational lensing does not pose a challenge for the idea that superfluid dark matter mimics modified gravity.

1 Introduction

Recently, a new theory of superfluid dark matter (SFDM) has been proposed as a possible solution of the missing-mass problem on both galactic and cosmological scales [1, 2]. While the idea that dark matter made of light particles might condense to a superfluid has been considered before on general grounds [3, 4, 5, 6, 7, 8, 9, 10, 11, 12], the type of superfluid proposed in [1, 2] has an important additional feature: The phonons of the superfluid give rise to a new force that resembles the force that was postulated decades ago in Modified Newtonal Dynamics (MOND) [13, 14, 15].

This type of theory hence occupies an awkward middle position between modified gravity and particle dark matter. The reason for this hybrid behavior is that on purely mathematical grounds the equations of the superfluid look very similar to those that were previously discussed as modified gravity. Indeed, it was shown in [16] that a holography-based ansatz to emergent gravity proposed in [17] results in a generally covariant theory very similar to the SFDM considered in [1, 2]. The major difference between the two cases is that the proposal in [17, 16] is based on a vector field, whereas [1, 2] use a scalar field. For the purposes of the present study, we use the scalar field.

In our perspective, it is therefore justified to also refer to the type of SFDM considered here as modified gravity because – if this theory is correct – then the force acting on stars that orbit galactic centers is not merely due to the gravitational pull of the additional field. The superfluid has a mass and hence exerts a gravitational pull, but what gives rise to the MOND-like properties is the additional phonon force. Gravity, hence, is indeed modified.

It is worthwhile to point out that in the not-superfluid phase the additional force does not exist, so that the field acts like normal cold dark matter whenever the temperature is too high or the potential is not deep enough to induce condensation to a superfluid. While it is not presently known how well this agrees with the data, this means there is no reason a priori to worry about the compatibility of the model considered here with other evidence usually attributed to dark matter, such as the height of the third acoustic peak of the cosmic microwave background or the dynamics of galactic clusters, because in neither case the conditions for condensation are fulfilled.

There is however one observation that springs to mind immediately which might pose a challenge to SFDM, which is gravitational lensing. The reason is the following.

We know from the detection of a gravitational wave event with optical counterpart [18] that gravitational waves travel at the same speed as photons to high precision. This means that the phonon force of the superfluid has a negligible, if any, effect on photons [19, 20]. This is not theoretically difficult to achieve; it simply means that the respective coupling term does not exist (or is highly suppressed). An easy way to achieve this would be, for example, to have a coupling that depends on the particle’s rest mass, in which case photons would remain entirely unaffected by the phonon force. A similar result could be obtained by postulating that the coupling be conformal. However, if the total force acting on photons is not the same as that acting on baryons, this means that the apparent dark matter inferred from the motion of baryons will generically not match the dark matter inferred from gravitational lensing.

The purpose of this present work is to test whether this mismatch can be detected by use of strong gravitational lensing. The answer, roughly speaking, is “No”: Strong gravitational lensing is not a promising way to probe whether SFDM mimics a MOND-like force. The rest of the paper will explain why that is so and what restrictions apply to this rough answer.

2 The Model

We here use the model from [2] in which the fluid is described by a massive, real, scalar field ϕ . At zero temperature, the Lagrangian has the form

$$\mathcal{L}_\phi = 2\Lambda \frac{(2m)^{3/2}}{3} \chi \sqrt{|\chi|}, \quad (1)$$

where χ is the kinetic term of the scalar field, m is a constant of dimension mass, and Λ quantifies the strength of the self-interaction. In the Newtonian limit the kinetic term can

be approximated by

$$\chi \approx \mu - m\Phi + \dot{\phi} - \frac{1}{2m}(\vec{\nabla}\phi)^2, \quad (2)$$

where Φ is the Newtonian gravitational potential and μ can be interpreted as the chemical potential. A dot, as usual, denotes a derivative with respect to time; the gradient contains spatial derivatives only.

In the same limit, the new field ϕ couples to the energy-density of baryons ρ_b through the interaction term

$$\mathcal{L}_{\text{int}} = \alpha \frac{\Lambda}{m_{\text{pl}}} \phi \rho_b, \quad (3)$$

where m_{pl} is the Planck mass (and only there for dimensional reasons), and α is a dimensionless constant that quantifies the strength of the interaction. It is the combination of the power 3/2 in the kinetic term (1) combined with the peculiar coupling (3) that gives rise to the MOND-like behavior. The same features can be found in the vector-based model considered in [16].

If one now derives the equations of motion for the field ϕ from the Lagrangian, the equations will depend on the Newtonian potential Φ . In addition, we have the usual Poisson-equation for Φ , sourced by the total energy density (ie that of baryons and ϕ combined). Assuming spherical symmetry, the differential equation for ϕ can be solved analytically and the differential equation for Φ can be readily numerically integrated. From the results one can then calculate the total force acting on the baryons, which is a combination of the gravitational pull (stemming from Φ) and the phonon force (from ϕ). Photons, on the other hand, merely see the gravitational potential Φ .

There is however, an additional complication in this model, which is that at finite temperature the fluid will consist of two components, one that is superfluid and one that behaves like a normal fluid. To deal with this difficulty, we will follow here the procedure proposed in [1, 2] and use the following modification of the zero-temperature Lagrangian (see also [21])

$$\mathcal{L}_\phi = 2\Lambda \frac{(2m)^{3/2}}{3} \chi \sqrt{|\chi - b\Upsilon|}, \quad (4)$$

where

$$\Upsilon := \mu - m\Phi + \dot{\phi} + \vec{v} \cdot \vec{\nabla}\phi, \quad (5)$$

and \vec{v} is the velocity vector of the normal fluid component. As in Refs. [1, 2] we will in the following work in the normal-fluid rest-frame, i.e. we take $\vec{v} = 0$. Note that this choice of Lagrangian also cures a ghost in the zero-temperature model [1]. We will use the Lagrangian (4) up to the thermal radius, as laid out in [2], and then match the superfluid's density profile to a standard NFW profile [22].

We use the parameter values $b = 2$, $\alpha = 5.7$, $m = 1 \text{ eV}$, and $\Lambda = 0.05 \cdot 10^{-3} \text{ eV}$ as in [2]. The chemical potential, μ , takes on different values for different galaxies as further discussed in Sec. 4.

With the so specified model, we can then calculate both the profile of the phonon field as well as the gravitational potential from the initial conditions of the fields. This gives us the actual gravitational mass, consisting of both baryons and the energy-density of ϕ – which is what affects the trajectories of photons – and we can also calculate the total force acting on the baryons, composed of the gravitational force and the phonon force. Our procedure will then be to see whether we can find any initial conditions that fit the data of the strong gravitational lenses.

3 Data

In Ref. [2], the effect of SFDM on baryonic matter was tested by fitting rotation curves of two galaxies (the low surface-brightness galaxy IC 2574 and the high surface-brightness galaxy UGC 2953). Here, we are interested in the effect of SFDM on both photons and baryons. To this end, we will consider both the velocity dispersion and the Einstein radius of a set of 65 lenses from the Sloan Lens ACS (SLACS) Survey. These lenses are classified as ellipticals and have velocity dispersions from SDSS measurements as well as complete photometric data from Hubble Space Telescope (HST) measurements. We have taken the redshifts, Einstein radii, effective radii, and velocity dispersions from Ref. [23] and the aperture radius and seeing from Ref. [24].

This is the same set of lenses that was previously studied in Ref. [25] to evaluate the compatibility of these lenses with MOND. This previous study however only took into account the Einstein radius (and demonstrated that fitting it can be achieved with MOND). Our analysis improves on this previous work because we will investigate whether we can fit both the Einstein radius *and* the velocity dispersion at the same time to address the worry that this may not be possible if photons and baryons feel different forces.

The most interesting case would be to compare the gravitational mass $M(r)$ inside some sphere with radius r to the mass inferred from kinematic measurements at the same radius. However, with the measurements of the strong lensing systems from Ref. [25] this is not possible for two reasons. First, measurements of the Einstein radius R_E depend on the gravitational mass $M_E(R_E)$ inside a cylinder along the line of sight rather than the mass inside a sphere with radius R_E . Second, for the galaxies considered here [24, 23] only averaged velocity dispersions are available, hence we cannot resolve a radial dependence.

Nevertheless, as a first check we should find out whether the Einstein radii and the velocity dispersions can be fit at the same time with SFDM, and this will be our main task in the present work.

4 Calculation

For our calculations, we follow Ref. [25] in assuming spherical symmetry and a Jaffe mass distribution for the baryons [26]. Specifically, we take the baryonic energy density $\rho_b(r)$ to be of the form

$$\rho_b(r) = \frac{M_b}{4\pi R_J} \frac{1}{r^2(1+r/R_J)^2}. \quad (6)$$

Here, M_b is the total baryonic gravitational mass and $R_J = 1.31 R_{\text{eff}}$ is derived from the effective radius $R_{\text{eff}} = \Theta_{\text{eff}} \cdot D_l$ with the angular effective radius Θ_{eff} and the angular distance of the lens D_l [26]. For each galaxy, the effective radius of the Jaffe model is thereby determined from measurements. This leaves the total baryonic mass, M_b , as the only free parameter of the baryonic mass distribution which is one of two free parameters we will use to fit the data.

As briefly laid out in section 2, the first step to calculate the Einstein radius and the velocity dispersion is solving the equations of motion of the phonon field ϕ and the gravitational potential Φ . This is described in detail in Sec. V of Ref. [2]. Here, we only clarify a few points regarding the required initial conditions for the gravitational field. With the analytic solution for ϕ , the resulting Poisson equation for Φ inside the superfluid phase reads

$$\frac{1}{r^2} \partial_r (r^2 \partial_r \Phi(r)) = 4\pi G [\rho_b(r) + \rho_{\text{SF}}(a_b(r), \hat{\mu}(r))]. \quad (7)$$

Here, $a_b(r)$ is given by $GM_b(r)/r^2$ with the baryonic mass $M_b(r)$ inside the sphere with radius r , ρ_{SF} is the energy density of the superfluid, and

$$\hat{\mu}(r) \equiv \mu - m\Phi(r). \quad (8)$$

Eq. 7 can be rewritten so that it depends on Φ only indirectly through $\hat{\mu}$. This is because we can use $\hat{\mu}'(r) = -m\Phi'(r)$ on the left-hand side of Eq. 7 (where a prime denotes a derivative with respect to the radial coordinate r). This means that given initial conditions $\hat{\mu}(r_0)$ and $\hat{\mu}'(r_0)$ for some r_0 , the resulting equation can be solved numerically for $\hat{\mu}(r)$. With this procedure we can obtain $\Phi'(r)$ (but not $\Phi(r)$) without specifying μ and $\Phi(r_0)$ separately, only the combination $\hat{\mu}(r_0) = \mu - m\Phi(r_0)$ is required.

In our calculations, we only need $\Phi'(r)$ but not $\Phi(r)$. Therefore, we follow the procedure described in the previous paragraph and take the quantity $\hat{\mu}(r_0)$ as the second free parameter in our calculation. Since we will integrate the equations numerically, we take $r_0 = 0.01 \text{ kpc} > 0$ in order to avoid difficulties with solving the Poisson equation at $r = 0$. The other initial condition for the Poisson equation in spherical coordinates is usually $\hat{\mu}'(r = 0) = 0$. But since we solve the Poisson equation only for $r \geq r_0 > 0$, we instead take as our second initial condition $\hat{\mu}'(r_0) = -m \cdot 4\pi G r_0 (\rho_b(r_0) + \rho_{\text{SF}}(r_0))$ which is obtained by expanding $\hat{\mu}'(r)$ for small r .

The next step consists in determining the radius at which the superfluid phase ends and the particle dark matter phase begins. In Ref. [2], two algorithms were offered to determine this radius. For simplicity, we will here take the thermalization radius R_T as an estimate for the radius at which the superfluid phase ends. According to Sec. III of Ref. [2] this radius is determined from

$$\Gamma = t_{\text{dyn}}^{-1}, \quad (9)$$

where Γ is the local self-interaction rate and t_{dyn} is the dynamical time.

We can estimate the thermal radius by using $\Gamma = (\sigma/m) \mathcal{N} v \rho$, where σ is the self-interaction rate, $\mathcal{N} = (\rho/m)(2\pi/mv)^3$ is the Bose-degeneracy factor, and v is the average velocity of the particles. As in Ref. [2], we take $\sigma/m = 0.01 \text{ cm}^2/\text{g}$. Similarly, we can estimate $t_{\text{dyn}} \approx r/v$ and $v^2 \approx r \cdot \Phi'(r)$. Inserting these expressions into (9) allows one to obtain the thermalization radius R_T .

This procedure is arguably somewhat ad-hoc and good only approximately. Ideally one would want to be able to derive the composition of the two fluid-components as a function of radius (or pressure, respectively) directly from the Lagrangian. We have checked, however, that our results do not depend much on the exact numerical factors in the above estimate and our general conclusion is not affected. That the exact numerical factors do not affect our conclusion is supported by the analysis in Sec. 6.4, where we have explicitly tried an alternative procedure for matching the superfluid core to an NFW halo.

Further, following Refs. [1, 2], we assume that outside the superfluid phase, the energy-density of the new field follows an NFW profile. For simplicity, we approximate this NFW profile ρ_{NFW} outside the superfluid phase as $\rho_{\text{NFW}} \propto 1/r^3$ (though we checked that our results do not strongly depend on the exact form of the potential).

For the calculation of the angular Einstein radius Θ_E , we follow Ref. [27] and fix the post-Newtonian parameter γ at its GR value $\gamma \equiv 1$ so that Θ_E is determined by

$$\Theta_E^2 = \frac{D_{\text{ls}}}{D_1 D_s} 4 G M_E(R_E), \quad (10)$$

$$R_E = D_1 \Theta_E, \quad (11)$$

where G is Newton's gravitational constant, R_E is the Einstein radius, and D_1 , D_s , and D_{ls} are the angular distances of the lens, the source, and the angular distance between the source and the lens, respectively. Further, $M_E(R_E)$ denotes the gravitational mass inside the cylinder with radius R_E along the line of sight.

For the calculation of the radial velocity dispersion σ_r , we need to modify the formalism of Ref. [27] due to the additional phonon force which acts on the baryons. To this end, consider the formula for the velocity dispersion from Ref. [27]

$$\sigma_r^2(r) = \frac{G \int_r^\infty dr' \rho_b(r') M_\sigma(r') (r')^{2\beta-2}}{r^{2\beta} \rho_b(r)}, \quad (12)$$

with the anisotropy parameter β , the baryonic energy density $\rho_b(r)$ and the mass $M_\sigma(r)$. Here, $M_\sigma(r)$ is calculated from the total acceleration of the baryons $a_{\text{tot}}(r)$ according to

$$\frac{GM_\sigma(r)}{r^2} = a_{\text{tot}}(r). \quad (13)$$

We stress that $a_{\text{tot}}(r)$ is the total acceleration which must include accelerations other than the gravitational acceleration if present. This can be seen by rederiving this formula for σ_r following Ref. [28] in the case with forces other than the gravitational force acting on the baryons.

As already mentioned above, SFDM predicts that $a_{\text{tot}}(r)$ contains a contribution $a_\phi(r)$ from the phonon force in addition to the usual gravitational acceleration $a_{\text{grav}}(r)$:

$$\frac{GM_\sigma(r)}{r^2} = a_{\text{grav}}(r) + a_\phi(r), \quad (14)$$

where $a_\phi(r)$ is given by

$$a_\phi(r) = \alpha \frac{\Lambda}{m_{\text{Pl}}} \phi'(r). \quad (15)$$

The measured velocity dispersion σ_* can then be obtained as in Ref. [27] by using Eq. 12 for σ_r with the modified mass $M_\sigma(r)$ from Eq. 14:

$$\sigma_*^2 = \frac{\int_0^\infty dR R w(R) \int_{-\infty}^\infty dz \rho_b(r) \left(1 - \beta \frac{R^2}{r^2}\right) \sigma_r^2(r)}{\int_0^\infty dR R w(R) \int_{-\infty}^\infty dz \rho_b(r)}, \quad (16)$$

$$w(R) = e^{-R^2/2\tilde{R}_{\text{atm}}^2}, \quad (17)$$

$$\tilde{R}_{\text{atm}} = \tilde{\sigma}_{\text{atm}} D_1, \quad (18)$$

$$\tilde{\sigma}_{\text{atm}} = \sigma_{\text{atm}} \sqrt{1 + \theta_{\text{ap}}^2/4 + \theta_{\text{ap}}^4/40}. \quad (19)$$

Here, $r = \sqrt{R^2 + z^2}$, σ_{atm} is the seeing, and θ_{ap} is the spectrometric aperture. In particular, we have $\sigma_{\text{atm}} = 1.4''$ and $\theta_{\text{ap}} = 1.5''$ [24]. For simplicity, we take $\beta = 0$.

Angular distances D in the calculations for both the Einstein radius and the velocity dispersion are determined from the measured redshifts z_1 and z_2 of the lens and the source, respectively. More concretely, we employ the relation

$$D(z_1, z_2) = \frac{1}{H(1+z_2)} \int_{z_1}^{z_2} \frac{dz'}{\sqrt{\Omega_m(1+z')^3 + (1-\Omega_m)}}, \quad (20)$$

where z_1 and z_2 are the redshifts of the objects whose angular distance is to be calculated. Further, we take $H = 70 \text{ km s}^{-1} \text{ Mpc}^{-1}$ and $\Omega_m = 0.3$ following Ref. [23].

5 Fitting procedure

We now search for values of the two parameters – the baryonic mass M_b and $\hat{\mu}(r_0)$ – that can reproduce both the measured Einstein radius and the measured velocity dispersion of each galaxy. This search proceeds as follows.

First, we fix M_b at a starting value, for which we use the mass M_J listed in Ref. [25]. Next, we scan different values of $\hat{\mu}(r_0)$, starting at $0.5 \cdot 10^{-5}$ eV until we find a value for which Eq. 9 has a solution and the calculated Einstein radius R_E^{calc} matches the measured Einstein radius R_E^{meas} to at least 0.01 kpc. The step size of $\hat{\mu}(r_0)$ starts at $0.3 \cdot 10^{-5}$ eV and is decreased each time $R_E^{\text{calc}} - R_E^{\text{meas}}$ switches sign with a minimum step size of $0.005 \cdot 10^{-5}$ eV.

If we do not find a value of $\hat{\mu}(r_0)$ with $|R_E^{\text{calc}} - R_E^{\text{meas}}| < 0.01$ kpc, we decrease M_b by $0.25 \cdot 10^{11} M_\odot$ and repeat the previous step. We iterate this procedure until the measured Einstein radius is matched.

With the values of M_b and $\hat{\mu}(r_0)$ obtained in this way, we then calculate the velocity dispersion σ_*^{calc} and compare it to the measured value σ_*^{meas} . If σ_*^{calc} is closer to σ_*^{meas} than the error σ_*^{error} cited in Ref. [23], we take this galaxy to be successfully fitted. If not, we go back to the previous step, but instead of setting $M_b = M_J$ we increase or decrease M_b by $0.25 \cdot 10^{11} M_\odot$ depending on whether σ_*^{meas} is larger or smaller than σ_*^{calc} .

In this way, we obtain one value of M_b and $\hat{\mu}(r_0)$ for each galaxy. For some galaxies, these values correspond to a successful fit, for others they are the closest we could match the measured velocity dispersion so far.

We then proceed to scan values of M_b with a finer resolution. In particular, we take the value for M_b obtained in the previous steps and scan both larger and smaller values of M_b in steps of $0.05 \cdot 10^{11} M_\odot$. For each value of M_b we re-adjust $\hat{\mu}(r_0)$ to fit the Einstein radius and then check whether or not the calculated velocity dispersion matches with the measured one.

For some galaxies, this procedure produces a list of values of M_b and $\hat{\mu}(r_0)$ which fit both the Einstein radius as well as the velocity dispersion. For galaxies for which we do not obtain a successful fit, we nevertheless record the values of M_b and $\hat{\mu}(r_0)$ which give the closest match of the measured velocity dispersion.

Note that the above procedure only fully exploits the measurement errors in the velocity dispersion. The Einstein radius is always matched to 0.01 kpc which is usually less than the percent-level measurement error [24]. Consequently, there may be additional values of M_b and $\hat{\mu}(r_0)$ which also fit some galaxies but which we do not find since we do not exploit the measurement errors on the Einstein radius. However, we noticed that varying the Einstein radius by a few percent does not lead to qualitatively new results. In particular, most parameters only vary by a few percent as a result of changing the Einstein radius by a few percent. The only exception is the non-baryonic gravitational mass M_{DM} inside the virial radius r_{200} . As discussed below, this parameter is very sensitive to the other parameters so it is expected that it varies significantly when varying the Einstein radius.

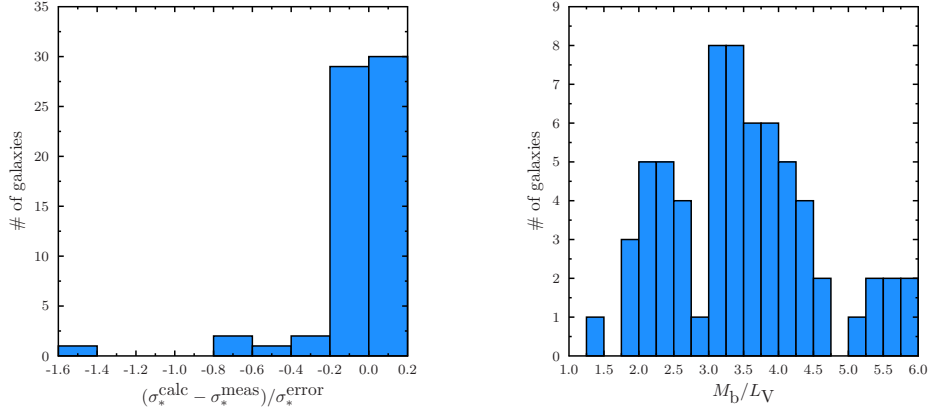


Figure 1: Left: Histogram of the $(\sigma_*^{\text{calc}} - \sigma_*^{\text{meas}})/\sigma_*^{\text{error}}$ with minimum absolute value for each galaxy. Right: Histogram of the calculated stellar mass-to-light-ratios for M_b and $\hat{\mu}(r_0)$ such that $|\sigma_*^{\text{calc}} - \sigma_*^{\text{meas}}|$ is minimal.

It is important to note that for this procedure we require that a solution for Eq. 9 exists. This means we enforce the existence of a superfluid phase in equilibrium. This implies that if the parameters of a galaxy are such that they do not admit a superfluid phase in equilibrium, we will not be able to successfully fit this galaxy. Or, to put it differently, if we cannot fit a galaxy it might mean this galaxy does not contain a superfluid phase.

We performed the calculation and the above described fitting procedure in Mathematica [29].

6 Results

The results of our calculation are summarized in Table 1 and Figs. 1, 2, and 3. It can be seen from Fig. 1, left, that we are able to successfully fit 64 out of 65 galaxies. The stellar mass-to-light ratios, M/L_V , of the fitted galaxies are reasonable, see Fig. 1, right. They are generally somewhat lower than those found in Ref. [25] for MOND: We find an averaged M/L_V of 3.5 ± 1.1 compared to the 4.2 ± 1.0 obtained in Ref. [25].

Assuming a Salpeter and a Chabrier initial mass function (IMF), Ref. [23] gives an estimate of the total stellar mass of each galaxy which we can compare to the M_b obtained from our fitting procedure. To this end, we follow Ref. [25] and use our Jaffe mass model with the measured effective radius to calculate the stellar mass inside the measured Einstein radius. This can be done for our fitted M_b as well as for the stellar mass estimate from each IMF. The results are shown in Fig. 2. It can be seen that the Salpeter IMF tends to give stellar masses larger than our M_b , while the Chabrier IMF

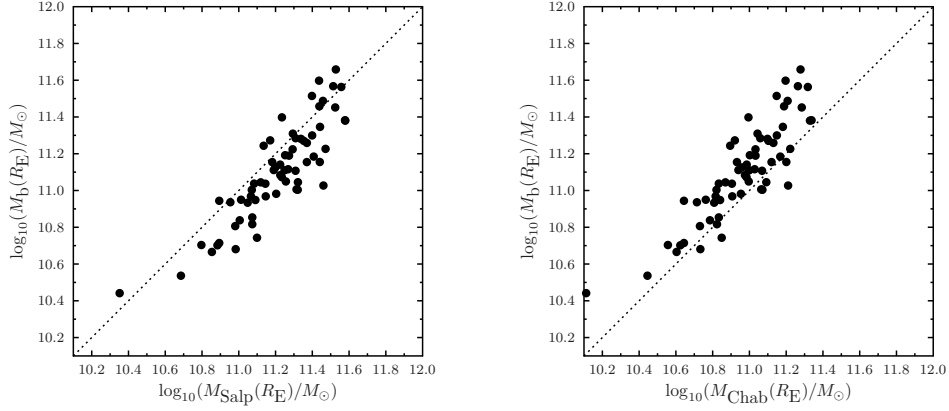


Figure 2: Left: Stellar mass within the cylinder with radius R_E^{meas} as calculated with the stellar mass estimated from the Salpeter IMF compared to that calculated with our M_b . Right: The same as left, but with the Chabrier IMF instead of the Salpeter IMF.

tends to give stellar masses smaller than our M_b . This again shows that our fitted stellar masses are reasonable.

6.1 Contribution of phonon force

To find out how much the phonon force contributes to σ_*^{calc} , we have also calculated a velocity dispersion $\sigma_*^{\text{calc, no}\phi}$ with $a_\phi \equiv 0$. As can be seen from Fig. 3, right, the phonon force contributes around 10% to the calculated velocity dispersion σ_*^{calc} .

At first sight it might seem surprising that the phonon force does not make a larger contribution to σ_*^{calc} since the phonon force is responsible for the MOND-like behavior discussed in Refs. [1, 2]. One therefore might expect that it should dominate over the gravitational force at least in a good part of each galaxy.

In order to understand the small contribution of the phonon force to σ_*^{calc} , we can approximate the phonon field $\phi'(r)$ by the expression it takes in the MOND-regime [1]

$$\phi'(r) = \sqrt{\frac{\alpha^3 \Lambda^2}{m_{\text{Pl}}} \frac{GM_b(r)}{r^2}}. \quad (21)$$

We can neglect the contributions of non-baryonic gravitational matter for reasons discussed in Sec. 6.2. From this, we can then derive analytic expressions for the contribution $\sigma_{r,\phi}^2(r)$ of the phonon force to $\sigma_r^2(r)$ and for the contribution $\sigma_{r,b}^2(r)$ of the gravitational force due to the baryons. The resulting expressions however are not very illuminating, so we will instead look at an example to see what is going on.

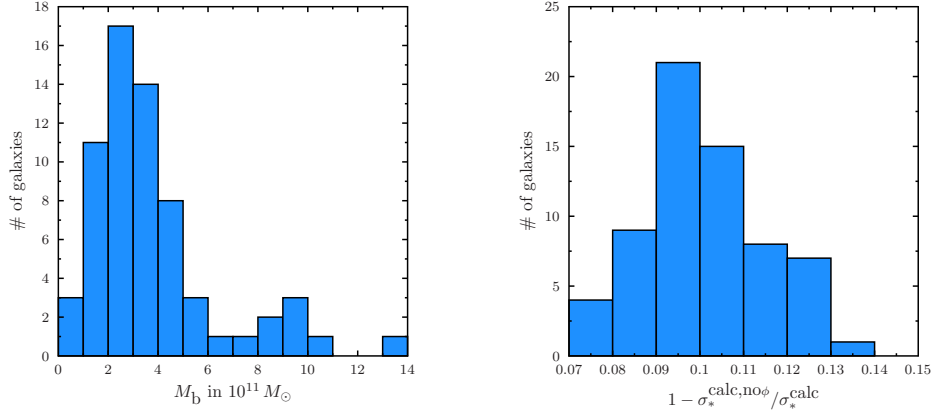


Figure 3: Left: Histogram of the total baryonic masses which lead to minimal $|\sigma_*^{\text{calc}} - \sigma_*^{\text{meas}}|$ for each galaxy. Right: Histogram of the fractions of σ_*^{calc} due to the phonon force for M_b and $\hat{\mu}(r_0)$ such that $|\sigma_*^{\text{calc}} - \sigma_*^{\text{meas}}|$ is minimal.

Fig. 4 shows both $\sigma_{r,b}^2(r)$ and $\sigma_{r,\phi}^2(r)$ for the galaxy J0029-0055. It can be seen that for most of the superfluid phase the phonon force is the dominant contribution to $\sigma_r^2(r)$. However, this is not true for small radii. Indeed, we find for $r \ll R_J$:

$$\sigma_{r,b}^2(r) \approx \frac{GM_b}{2R_J^2} (R_J - 4r), \quad (22)$$

$$\sigma_{r,\phi}^2(r) \approx \frac{2}{3} \alpha^{3/2} \Lambda \sqrt{\frac{GM_b}{m_{\text{Pl}} R_J}} r. \quad (23)$$

By plugging in typical numbers, one can confirm that in this regime the phonon force is usually smaller than the gravitational force exerted merely by the baryons.

In more detail, the reason for the relatively small contribution of the phonon force to σ_*^{calc} is that σ_*^{calc} is dominated by the contributions to $\sigma_r(r)$ that come from small r . According to Eq. 16, $(\sigma_*^{\text{calc}})^2$ is proportional to the weighted cylindrical integral over $\sigma_r^2(\sqrt{R^2 + z^2})$ with a weight factor proportional to $R \cdot \exp(-R/R_{\text{atm}}) \cdot \rho_b(\sqrt{R^2 + z^2})$. Both the exponential with $R_{\text{atm}} \sim 6 \text{ kpc}$ and the fall-off of ρ_b lead to $(\sigma_*^{\text{calc}})^2$ being mostly calculated from $\sigma_r^2(r)$ at radii where $\sigma_{r,\phi}^2(r)$ is small compared to $\sigma_{r,b}^2(r)$. Thus, the phonon force does not dominate the final result for σ_*^{calc} .

We want to emphasize that this finding agrees with the more general argument given in [25] that strong gravitational lensing is not sensitive to the distinction between MOND and cold dark matter because it mainly probes the mass in the galactic center which is dominated by baryons either which way. At small radii, the baryonic acceleration is larger than the MOND-acceleration scale a_0 . Therefore, the force acting on the baryons

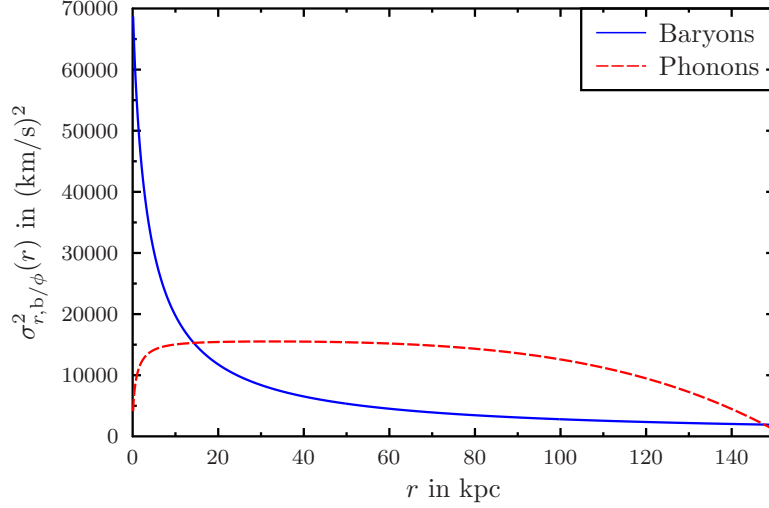


Figure 4: Different contributions to $\sigma_r^2(r)$ for the galaxy J0029-0055 inside the superfluid phase up to the galaxy's thermal radius $R_T \approx 153$ kpc. Shown is the phonon force approximated by its MOND-regime form $\sigma_{r,\phi}^2(r)$ and the contribution due to the gravitational pull of the baryons $\sigma_{r,b}^2(r)$.

should mainly be the gravitational force due to the baryons themselves.

6.2 Contribution of non-baryonic gravitational mass

Next, we would like to discuss how the non-baryonic gravitational mass contributes to the Einstein radius and the velocity dispersion.

First, consider the velocity dispersion. From Eq. 16 and Eq. 12 and leaving out the phonon force which was already discussed in Sec. 6.1, we have

$$\sigma_*^2 \propto \int_0^\infty dR R w(R) \int_{-\infty}^\infty dz \int_{\sqrt{R^2+z^2}}^\infty dr \rho_b(r) (M_b(r) + M_{\text{DM}}(r)), \quad (24)$$

$$M_b(r) \equiv \int_0^r dr' 4\pi r'^2 \rho_b(r'), \quad (25)$$

$$M_{\text{DM}}(r) \equiv \int_0^r dr' 4\pi r'^2 \rho_{\text{DM}}(r'). \quad (26)$$

Here, $\rho_{\text{DM}}(r)$ is the same as $\rho_{\text{SF}}(r)$ for $r < R_T$ and is proportional to $1/r^3$ for $r > R_T$. Eq. 24 implies that the relative size of the baryonic and the non-baryonic contributions to σ_* is determined by the relative size of $M_b(r)$ and $M_{\text{DM}}(r)$, i.e. the baryonic and the non-baryonic mass inside a sphere with radius r .

In contrast to this, the relative size of the baryonic and the non-baryonic contributions to the Einstein radius R_E is determined by the relative size of the baryonic and the non-baryonic mass inside a cylinder with radius R_E . More precisely, according to Eq. 10:

$$R_E^2 \propto M_{E,b}(R_E) + M_{E,DM}(R_E), \quad (27)$$

$$M_{E,b}(R) \equiv \int_0^R dR' \int_{-\infty}^{\infty} dz 2\pi R' \rho_b(\sqrt{R'^2 + z^2}), \quad (28)$$

$$M_{E,DM}(R) \equiv \int_0^R dR' \int_{-\infty}^{\infty} dz 2\pi R' \rho_{DM}(\sqrt{R'^2 + z^2}). \quad (29)$$

We will now argue that the non-baryonic mass is negligible for the calculation of the velocity dispersion, but does affect the Einstein radius.

Regarding the velocity dispersion, note that the baryonic mass is negligible for large spherical radii since it is typically concentrated inside a few 10kpc for the galaxies considered here. Similarly, for small spherical radii, the mass of the superfluid halo is negligible compared to the baryonic mass¹ as illustrated in Fig. 5, top, for the galaxy J0029-0055. Since the velocity dispersion is mainly calculated from small spherical radii as discussed in Sec. 6.1, it follows that the non-baryonic mass can be neglected when calculating σ_* .

For the calculation of the Einstein radius, both small and large spherical radii contribute since the Einstein radius is determined by the mass inside a cylinder with radius R_E . This is especially important for the non-baryonic matter $M_{E,DM}(R_E)$ since there is much more non-baryonic matter than baryonic matter in total, but most of this non-baryonic matter is located at large spherical radii. This is illustrated in Fig. 5, bottom. As a result, the non-baryonic matter $M_{E,DM}(R_E)$ is usually non-negligible for the calculation of the Einstein radius. In particular, for the galaxy J0029-0055, we have $M_{E,DM}(R_E)/M_{E,b}(R_E) \approx 10\%$.

6.3 Sensitivity of M_{DM} to initial condition

In this subsection, we will comment on one peculiarity in our results. Namely, the total non-baryonic gravitational mass M_{DM} is quite sensitive to the parameters $\hat{\mu}(r_0)$ and M_b . This regards the non-baryonic gravitational mass in the superfluid phase M_{DM}^{SF} as well as that outside the superfluid phase M_{DM}^{NFW} . For example, for the galaxy J0029-0055 the ratio of the maximum value $M_{DM}|_{\max}$ of M_{DM} to the respective minimum value $M_{DM}|_{\min}$ is about 200. This is despite the fact that the values of $\hat{\mu}(r_0)$ corresponding to the maximum and minimum M_{DM} differ only by a factor of about 1.6 and the values of M_b corresponding to the maximum and minimum M_{DM} differ only by a factor of about 0.8. We will now try to understand where this sensitivity comes from.

¹This can be checked explicitly by using the MOND-regime form of ϕ' from Eq. 21 in $\rho_{SF}(r) = 2/3m^2\Lambda(6m\hat{\mu}(r) + \phi'(r)^2) / \sqrt{2m\hat{\mu}(r) + \phi'(r)^2}$ with values of $\hat{\mu}$ close to their initial values listed in Table 1.

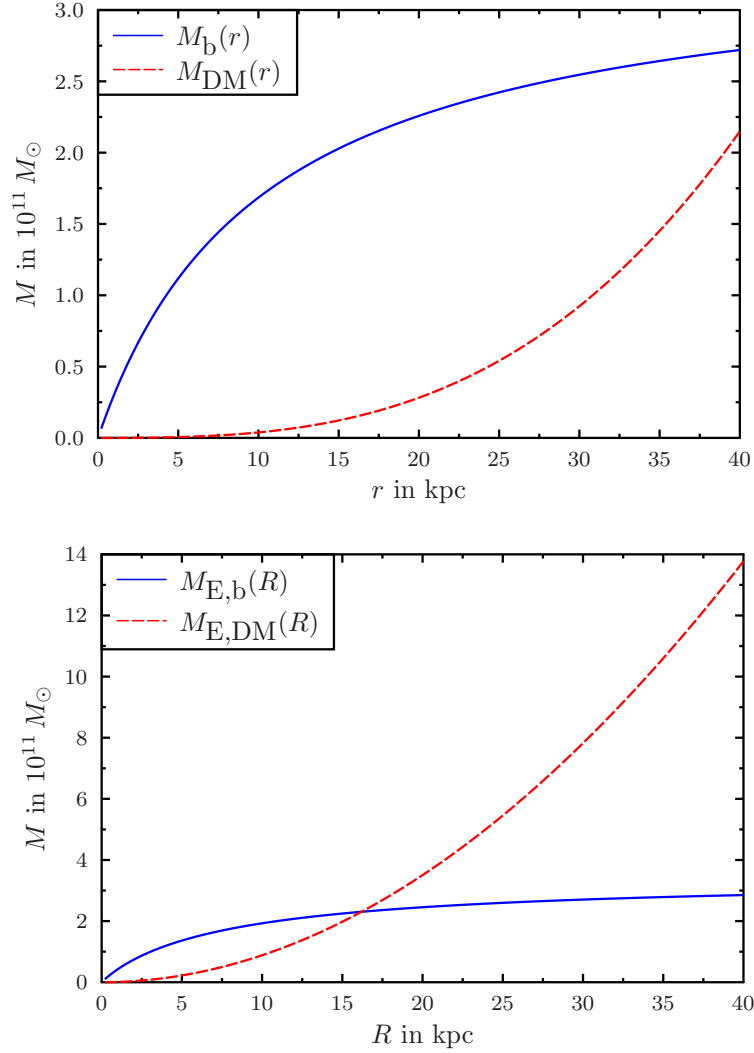


Figure 5: Top: The baryonic and non-baryonic gravitational masses $M_b(r)$ and $M_{DM}(r)$ inside a sphere with radius r for the galaxy J0029-0055. Bottom: The non-baryonic gravitational masses $M_{E,b}(R)$ and $M_{E,DM}(R)$ inside a cylinder with radius R for the galaxy J0029-0055.

Numerically, for the galaxy J0029-0055, the differences in $\hat{\mu}(r_0)$ and M_b imply a factor of about 2.9 in the thermal radius R_T and a factor of 3.3 in the average value of the non-baryonic energy density inside the superfluid phase ρ_{SF} . Thus, those quantities do not seem to be particularly sensitive to M_b and $\hat{\mu}(r_0)$.

Let us now consider the non-baryonic gravitational mass in the superfluid phase $M_{\text{DM}}^{\text{SF}}$. For our purposes, it suffices to approximate ρ_{SF} as constant which gives

$$M_{\text{DM}}^{\text{SF}} \sim \frac{4\pi}{3} R_T^3 \rho_{\text{SF}}. \quad (30)$$

With the numerical values cited above, this implies a ratio between the maximum and minimum values of $M_{\text{DM}}^{\text{SF}}$ of about 80. The actual value from the full calculation is 120 which is of the same order of magnitude.

A similar estimate is possible for the non-baryonic gravitational mass outside the superfluid phase $M_{\text{DM}}^{\text{NFW}}$ if we approximate the virial radius r_{200} as the radius at which the non-baryonic energy density drops below $\rho_{200} \equiv 200 \cdot 3H^2 / (8\pi G)$. Here, H is the Hubble rate. With this we obtain:

$$M_{\text{DM}}^{\text{NFW}} \sim \frac{4\pi}{3} R_T^3 \rho_{\text{SF}}(R_T) \ln \left(\frac{\rho_{\text{SF}}(R_T)}{\rho_{200}} \right). \quad (31)$$

With R_T as cited above and using $\rho_{\text{SF}}(R_T)|_{\min} = 1.2 \cdot 10^{-26} \text{ g/cm}^3$ as well as $\rho_{\text{SF}}(R_T)|_{\max} = 5.9 \cdot \rho_{\text{SF}}(R_T)|_{\min}$, this implies a ratio of the maximum and minimum values of $M_{\text{DM}}^{\text{NFW}}$ of about 280. The actual value from the full calculation is 230 which is again of the same order of magnitude.

Thus, while R_T and ρ_{SF} are not particularly sensitive to the values of $\hat{\mu}(r_0)$ and M_b , Eq. 31 and Eq. 30 show that the total non-baryonic gravitational mass is indeed quite sensitive to these values.

So far, it is not well-understood how the cosmological case works with SFDM, so that it is not clear if our values for M_{DM} would fit the cosmological data. Nevertheless, it is interesting to compare our results to Λ CDM abundance matching expectations. In Fig. 6, we show our results for M_b/M_{DM} together with the Λ CDM expectations determined by the following equation from Ref. [30]:

$$\left(\frac{M_b}{M_{\text{DM}}} \right)_{\Lambda\text{CDM}} = 2N \left[\left(\frac{M_{\text{DM}}}{M_1} \right)^{-\beta} + \left(\frac{M_{\text{DM}}}{M_1} \right)^{\gamma} \right]^{-1}. \quad (32)$$

Here, N , M_1 , β , and γ are redshift-dependent numbers which we take from Eqs. (11)-(14) and Table 1 of Ref. [30]. We see that most of our galaxies have $M_{\text{DM}} \gtrsim 10^{14} M_{\odot}$ and the corresponding values of M_b/M_{DM} are very roughly compatible with the Λ CDM values. In contrast, for galaxies with $M_{\text{DM}} \lesssim 10^{13} M_{\odot}$ we obtain significantly higher M_b/M_{DM} than Λ CDM. While this is interesting, we cannot draw any further conclusion from this without a cosmological model for SCDM.

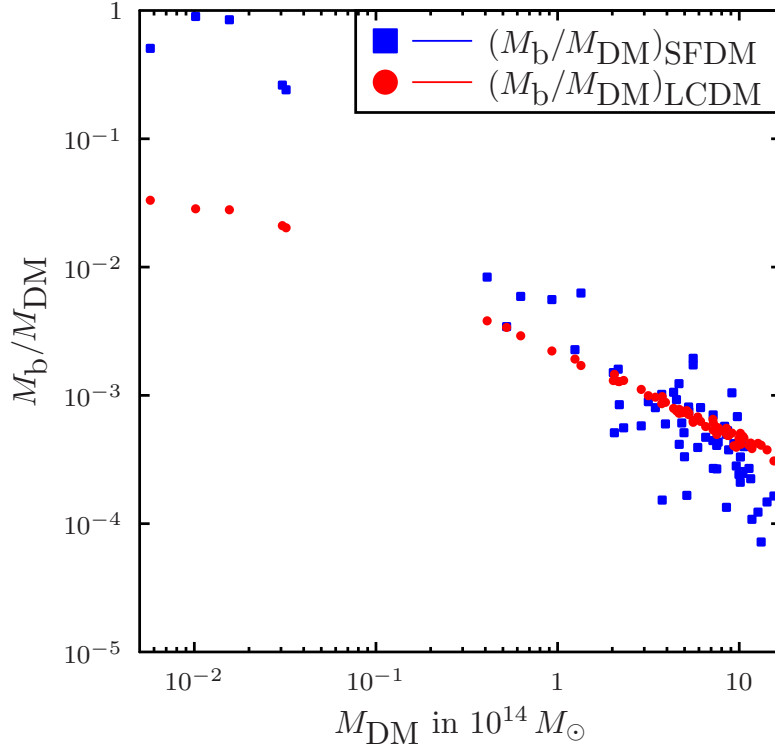


Figure 6: The ratio of stellar and halo mass over the halo mass, both for our calculations and for the Λ CDM mass-concentration relation given our M_{DM} .

6.4 Alternative NFW halo matching

Above, we used the thermal radius R_T as the radius where we match the superfluid core to an NFW tail. In Ref. [2], an alternative transition radius R_{NFW} was proposed. We will now look at this for completeness to check whether it makes a difference for our conclusions.

This radius R_{NFW} is defined by requiring that both the superfluid density and pressure match the respective density and pressure of the NFW halo. Further, Ref. [2] did not approximate the NFW halo to be proportional to $1/r^3$ but used the full NFW profile,

$$\rho_{NFW}(r) = \frac{\rho_c}{(r/r_s)(1+r/r_s)^2}, \quad (33)$$

where ρ_c and r_s are constants. This matching approach requires three parameters, namely

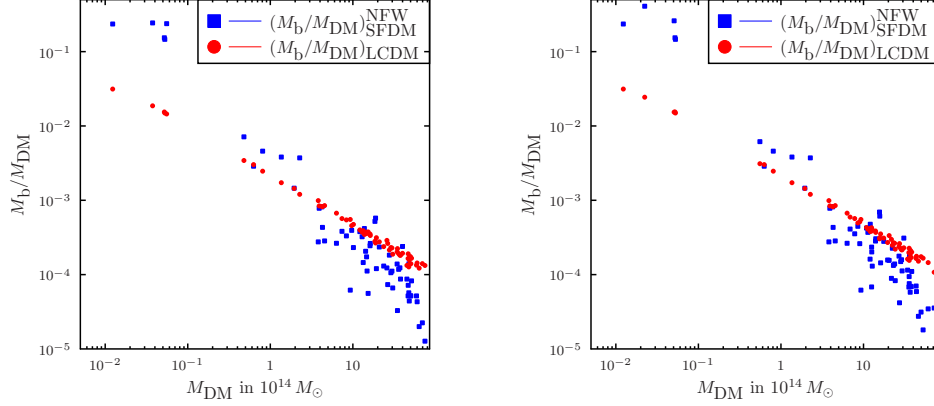


Figure 7: Left: Same as Fig. 6, but with NFW matching instead of thermal matching and with M_b and $\hat{\mu}(r_0)$ fixed at the values from the fitting procedure with thermal matching. Right: Same as Fig. 6, but with NFW matching instead of thermal matching and with σ_* and R_E fixed at the values from the fitting procedure with thermal matching.

ρ_c , r_s , and R_{NFW} . Requiring the density and pressure inside and outside the superfluid phase to match fixes only two of those.

In Ref. [2], the third parameter is fixed by choosing the concentration parameter $c = r_{200}/r_s$ according to the Λ CDM Mass-concentration relation of Ref. [31], with the Λ CDM halo mass identified with the calculated M_{DM} . In the following, we will call this procedure ‘NFW matching’ while we refer to the previously discussed procedure as ‘thermal matching’.

We will now explore how this alternative NFW matching affects our results. In particular, we will compare NFW-matching to thermal matching in two different cases. In the first case, we fix the superfluid core, i.e. the values of M_b and $\hat{\mu}(r_0)$, and then match a halo to this superfluid core with both matching procedures. In the second case, we fix the calculated velocity dispersion and Einstein radius, but allow the superfluid core to vary.

For the case with a fixed superfluid core, we take the values of M_b and $\hat{\mu}(r_0)$ as the best-fit values from the thermal matching procedure. The resulting values of M_b/M_{DM} from NFW matching are shown in Fig. 7, left. Comparing to the result from thermal matching in Fig. 6, we see that NFW matching gives larger M_{DM} values than thermal matching. Averaging over all galaxies, we find $M_{\text{DM}}^{\text{NFW}}/M_{\text{DM}}^{\text{thermal}} = 3.4 \pm 1.3$, where $M_{\text{DM}}^{\text{NFW}}$ denotes the values of M_{DM} obtained with NFW matching and $M_{\text{DM}}^{\text{thermal}}$ denotes those obtained with thermal matching. In Fig. 8, left, we see that the different matching procedures affect the calculated velocity dispersions only on the sub-percent level. This is because the velocity dispersions are dominated by the superfluid core which we have

kept constant. In contrast, the Einstein radii receive a larger contribution from the NFW halo. And indeed, the Einstein radii do change above the percent-level when switching to NFW matching, see Fig. 8, right. Averaging over all galaxies, the relative difference is 5.2 % with 9.1 % standard deviation.

For the case with fixed calculated velocity dispersion and Einstein radius, we similarly take these fixed values as the best-fit values from the thermal matching procedure. These fixed values of the velocity dispersion and the Einstein radius can be reached with NFW matching by keeping M_b fixed and adjusting $\hat{\mu}(r_0)$ in order to match the Einstein radius. This is possible since the velocity dispersion depends only very weakly on $\hat{\mu}(r_0)$ as discussed in Sec. 6.2. Therefore, keeping M_b fixed keeps the velocity dispersion fixed and adjusting $\hat{\mu}(r_0)$ effectively adjusts only the Einstein radius. Indeed, this procedure leads to velocity dispersions which agree with those from thermal matching to at least 1 %. Here, we adjust $\hat{\mu}(r_0)$ such that the Einstein radii differ by at most 0.01 kpc.

The resulting values of M_{DM} from NFW matching are again higher than with thermal matching, but a bit lower than in the case with a fixed superfluid core, see Fig. 7, right. We obtain $M_{\text{DM}}^{\text{NFW}}/M_{\text{DM}}^{\text{thermal}} = 2.8 \pm 0.8$. For all galaxies, the velocity dispersions and Einstein radii obtained with thermal matching can be reproduced with NFW matching. More precisely, our procedure reproduces the Einstein radii to at least 0.01 kpc and the velocity dispersions to at least 1 %. Therefore, NFW matching allows to fit the velocity dispersions and Einstein radii at least as good as thermal matching.

To sum up, using NFW matching instead of thermal matching has a relatively small effect on the calculated velocity dispersions and Einstein radii. Further, we can obtain the same velocity dispersions and Einstein radii as with thermal matching by adjusting M_b and $\hat{\mu}(r_0)$. In contrast, NFW matching leads to larger values of M_{DM} than thermal matching. However, when interpreting the values of M_{DM} , it should be kept in mind that M_{DM} is quite sensitive to the initial conditions as discussed in Sec. 6.3.

6.5 The galaxy J0737+3216

The galaxy J0737+3216 is the only galaxy in our sample for which we do not obtain a successful fit according to the procedure described in Sec. 5. The reason we do not obtain a fit is that, given the requirements $|R_E^{\text{calc}} - R_E^{\text{meas}}| < 0.01 \text{ kpc}$ and $|\sigma_*^{\text{calc}} - \sigma_*^{\text{meas}}| < \sigma_*^{\text{error}}$, no thermalization radius R_T can be determined since there is no solution to Eq. 9. This is because $\Gamma < t_{\text{dyn}}^{-1}$ for all radii which means that there is no superfluid phase in equilibrium. Therefore, it seems this galaxy should be modeled as having a standard cold dark matter halo at all radii instead of a superfluid halo at small radii and an NFW halo at large radii.

However, note that requiring a superfluid phase and $|R_E^{\text{calc}} - R_E^{\text{meas}}| < 0.01 \text{ kpc}$, we obtain $\sigma_*^{\text{calc}} = 314 \text{ km/s}$ which is not too far off the measured value $\sigma_*^{\text{meas}} = 338 \pm 16 \text{ km/s}$. Indeed, allowing for a 5 % error on R_E^{meas} , we are able to obtain a successful fit for J0737+3216. This implies that uncertainties in the measurements or our theoretical modeling could also be the reason for the lack of a successful fit for this galaxy. Hence, this galaxy does not provide a clear case of a galaxy that should be modeled as not having a

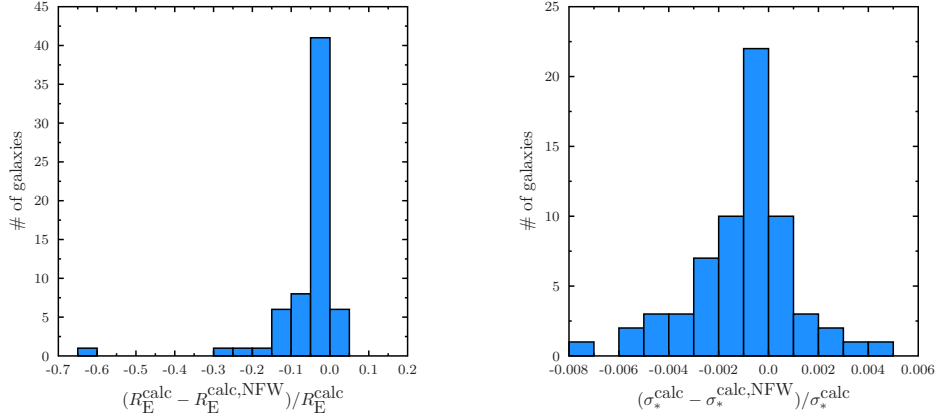


Figure 8: Left: Relative difference in the calculated Einstein radius between the thermal and NFW matching with M_b and $\hat{\mu}(r_0)$ fixed at the values from the fitting procedure with thermal matching. Right: Relative difference in the calculated velocity dispersion between the thermal and NFW matching with M_b and $\hat{\mu}(r_0)$ fixed at the values from the fitting procedure with thermal matching.

superfluid phase in SFDM.

Furthermore we wish to remind the reader that the whole ansatz we are using here for the superfluid in the galaxies relies on time-independence and spherical symmetry. This may quite possibly simply be a bad ansatz for some galaxies. For this reason we do not think the one outlier is the interesting part of our analysis. More interesting is that the model generally seems to work quite well, despite the worries that one might have had about phonons and baryons reacting to different forces.

6.6 Discussion

Strong lensing systems have generally been consistent with the gravitational mass inferred from lensing being equal to the mass inferred from kinematical measurements [32].

In SFDM, those two masses differ from each other because the phonon force makes a contribution to the kinematically inferred mass. Therefore, it is tempting to attribute the success of SFDM in fitting Einstein radii and velocity dispersions at the same time to the minor contribution of the phonon force to the velocity dispersion, as discussed in Sec. 6.1.

However, as our analysis reveals, the main reason for the success of SFDM in fitting the strong lensing systems is a different one: It is the possibility to independently adjust the Einstein radius R_E and the velocity dispersion σ_* through the two free parameters

of the superfluid in each galaxy. The first of the free parameters in our calculation is the total baryonic mass M_b which affects both the Einstein radius and the velocity dispersion. The second parameter $\hat{\mu}(r_0)$ determines the amount of the non-baryonic gravitational mass. The important point is that this non-baryonic mass is negligible in calculating the velocity dispersion and only affects the Einstein radius, as discussed in Sec. 6.2. As a consequence, we can independently adjust the Einstein radius and the velocity dispersion which allows us to fit the Einstein radius and the velocity dispersion at the same time.

It should be added at this point that in MOND a similar procedure would not be possible because in this case one has only one free parameter.

Finally, there may be other ways of testing the proposal of superfluid dark matter. The ansatz we studied here must have a UV-completion and as such will almost certainly give rise to new particles. Such particles can in principle be directly detected if their properties are understood well-enough. A proposal for a UV-completion has been discussed in [33], though much work remains to be done.

7 Conclusion

We have obtained successful fits with reasonable stellar mass-to-light ratios for both the Einstein radius and the velocity dispersion of 64 out of 65 strong gravitational lenses. Therefore, we conclude, strong lensing systems – at least of the type in our sample – do not seem to pose a challenge for superfluid dark matter.

Furthermore we have demonstrated that the averaged velocity dispersions of the considered galaxies probe the phonon force postulated by SFDM mainly at relatively small radii where it is subdominant compared to the gravitational force due to the baryons. As a result, the phonon force contributes only about 10% to the calculated velocity dispersion. For this reason, strong lensing generally – and not just in our sample – does not seem to be a promising method to tell apart standard cold dark matter from superfluid dark matter. A cleaner test of the SFDM prediction (that the gravitational mass and the mass inferred from kinematics should be different) would have to probe galaxies at smaller baryonic accelerations where the contributions from the phonon force are more important.

References

- [1] L. Berezhiani and J. Khoury, Phys. Rev. **D92**, 103510 (2015), arXiv:1507.01019.
- [2] L. Berezhiani, B. Famaey, and J. Khoury, (2017), arXiv:1711.05748.
- [3] P. Sikivie and Q. Yang, Phys. Rev. Lett. **103**, 111301 (2009), arXiv:0901.1106.
- [4] T. Noumi, K. Saikawa, R. Sato, and M. Yamaguchi, Phys. Rev. **D89**, 065012 (2014), arXiv:1310.0167.

- [5] S. Davidson and M. Elmer, *JCAP* **1312**, 034 (2013), arXiv:1307.8024.
- [6] H. J. de Vega and N. G. Sanchez, (2014), arXiv:1401.1214.
- [7] S. Davidson, *Astropart. Phys.* **65**, 101 (2015), arXiv:1405.1139.
- [8] A. H. Guth, M. P. Hertzberg, and C. Prescod-Weinstein, *Phys. Rev.* **D92**, 103513 (2015), arXiv:1412.5930.
- [9] A. Aguirre and A. Diez-Tejedor, *JCAP* **1604**, 019 (2016), arXiv:1502.07354.
- [10] P. S. B. Dev, M. Lindner, and S. Ohmer, *Phys. Lett.* **B773**, 219 (2017), arXiv:1609.03939.
- [11] J. Eby, M. Ma, P. Suranyi, and L. C. R. Wijewardhana, *JHEP* **01**, 066 (2018), arXiv:1705.05385.
- [12] S. Sarkar, C. Vaz, and L. C. R. Wijewardhana, *Phys. Rev.* **D97**, 103022 (2018), arXiv:1711.01219.
- [13] M. Milgrom, *Astrophys. J.* **270**, 384 (1983).
- [14] M. Milgrom, *Astrophys. J.* **270**, 365 (1983).
- [15] J. Bekenstein and M. Milgrom, *Astrophys. J.* **286**, 7 (1984).
- [16] S. Hossenfelder, *Phys. Rev.* **D95**, 124018 (2017), arXiv:1703.01415.
- [17] E. P. Verlinde, *SciPost Phys.* **2**, 016 (2017), arXiv:1611.02269.
- [18] B. P. Abbott *et al.*, *Astrophys. J.* **848**, L12 (2017), arXiv:1710.05833.
- [19] S. Boran, S. Desai, E. O. Kahya, and R. P. Woodard, *Phys. Rev.* **D97**, 041501 (2018), arXiv:1710.06168.
- [20] R. H. Sanders, (2018), arXiv:1805.06804.
- [21] A. Nicolis, (2011), arXiv:1108.2513.
- [22] J. F. Navarro, C. S. Frenk, and S. D. M. White, *Astrophys. J.* **490**, 493 (1997), arXiv:astro-ph/9611107.
- [23] M. W. Auger *et al.*, *Astrophys. J.* **705**, 1099 (2009), arXiv:0911.2471.
- [24] A. S. Bolton *et al.*, *Astrophys. J.* **682**, 964 (2008), arXiv:0805.1931.
- [25] R. H. Sanders, *Mon. Not. Roy. Astron. Soc.* **439**, 1781 (2014), arXiv:1310.6148.
- [26] W. Jaffe, *Mon. Not. Roy. Astron. Soc.* **202**, 995 (1983).

- [27] J. Schwab, A. S. Bolton, and S. A. Rappaport, *Astrophys. J.* **708**, 750 (2010), arXiv:0907.4992.
- [28] J. Binney, *Mon. Not. Roy. Astron. Soc.* **190**, 873 (1980).
- [29] Wolfram Research, Inc., *Mathematica*, Version 11.
- [30] B. P. Moster, T. Naab, and S. D. M. White, *Mon. Not. Roy. Astron. Soc.* **428**, 3121 (2013), arXiv:1205.5807.
- [31] A. A. Dutton and A. V. Macciò, *Mon. Not. Roy. Astron. Soc.* **441**, 3359 (2014), arXiv:1402.7073.
- [32] B. Famaey and S. S. McGaugh, *Living Reviews in Relativity* **15**, 10 (2012), arXiv:1112.3960.
- [33] S. Alexander, E. McDonough, and D. N. Spergel, *JCAP* **1805**, 003 (2018), arXiv:1801.07255.

Table 1: Results of our fitting procedure for each galaxy. For $\hat{\mu}(r_0)$, M_b , M_b/L_V and M_{DM} the notation a_{-c}^{+b} is used which means that a is the value which corresponds to the σ_*^{calc} closest to σ_*^{meas} . $a + b$ and $a - c$ are the values which correspond, respectively, to the maximum and minimum values which still give a successful fit for σ_* if such values exist, see Sec. 5. $f_\phi \equiv 1 - \sigma_*^{\text{calc, no}\phi} / \sigma_*^{\text{calc}}$ denotes the fraction the phonon force contributes to σ_*^{calc} .

Lens	R_E^{meas} kpc	σ_*^{meas} km/s	σ_*^{calc} km/s	$\hat{\mu}(r_0)$ 10^5 eV	M_b $10^{11} M_\odot$	M_b/L_V	M_{DM} $10^{14} M_\odot$	f_ϕ %
J0008-0004	6.59	193 ± 36	194_{-35}^{+35}	$4.07_{-0.71}^{+0.66}$	$2.71_{-1.10}^{+1.40}$	$2.2_{-0.9}^{+1.1}$	$9.63_{-3.53}^{+3.21}$	12
J0029-0055	3.48	229 ± 18	229_{-17}^{+6}	$1.35_{-0.16}^{+0.54}$	$3.42_{-0.55}^{+0.25}$	$3.6_{-0.6}^{+0.3}$	$0.41_{-0.40}^{+1.82}$	12
J0037-0942	4.95	279 ± 10	279_{-9}^{+9}	$3.77_{-0.30}^{+0.30}$	$4.27_{-0.30}^{+0.30}$	$3.1_{-0.2}^{+0.2}$	$5.26_{-1.28}^{+1.36}$	9
J0044+0113	1.72	266 ± 13	266_{-11}^{+6}	$2.17_{-0.52}^{+1.66}$	$2.83_{-0.25}^{+0.15}$	$3.9_{-0.3}^{+0.2}$	$1.25_{-1.24}^{+5.31}$	8
J0157-0056	4.89	295 ± 47	285_{-37}^{+0}	$1.89_{-0.01}^{+1.08}$	$8.00_{-2.35}^{+0.05}$	$4.6_{-1.4}^{+0.0}$	$0.03_{-0.02}^{+4.17}$	12
J0216-0813	5.53	333 ± 23	333_{-23}^{+23}	$4.63_{-0.90}^{+1.07}$	$10.85_{-1.60}^{+1.80}$	$4.1_{-0.6}^{+0.7}$	$5.58_{-3.89}^{+4.68}$	10
J0252+0039	4.40	164 ± 12	163_{-10}^{+12}	$4.49_{-0.40}^{+0.33}$	$1.27_{-0.20}^{+0.25}$	$1.9_{-0.3}^{+0.4}$	$11.75_{-1.69}^{+1.40}$	12
J0330-0020	5.45	212 ± 21	212_{-20}^{+19}	$3.74_{-0.42}^{+0.42}$	$2.01_{-0.40}^{+0.45}$	$1.8_{-0.3}^{+0.4}$	$7.52_{-2.08}^{+2.04}$	10
J0728+3835	4.21	214 ± 11	213_{-10}^{+11}	$4.42_{-0.48}^{+0.42}$	$2.41_{-0.25}^{+0.30}$	$2.3_{-0.2}^{+0.3}$	$9.96_{-1.99}^{+1.77}$	10
J0737+3216	4.66	338 ± 16	314	2.37	7.71	3.6	0.03	10
J0819+4534	2.73	225 ± 15	225_{-15}^{+14}	$2.38_{-0.74}^{+1.05}$	$2.82_{-0.40}^{+0.40}$	$4.0_{-0.6}^{+0.6}$	$3.16_{-2.41}^{+3.71}$	11

Strong lensing with superfluid dark matter

J0822+2652	4.45	259 ± 15	259 ⁺¹⁵ ₋₁₄	3.25 ^{+0.59} _{-0.52}	4.18 ^{+0.55} _{-0.50}	3.5 ^{+0.5} _{-0.4}	4.51 ^{+2.43} _{-2.11}	10
J0903+4116	7.23	223 ± 27	223 ⁺²⁶ ₋₂₆	4.29 ^{+0.48} _{-0.50}	3.93 ^{+1.20} _{-1.05}	1.9 ^{+0.6} _{-0.5}	9.34 ^{+2.55} _{-2.66}	12
J0912+0029	4.58	326 ± 12	326 ⁺¹¹ ₋₁₂	5.45 ^{+0.77} _{-0.72}	9.54 ^{+0.75} _{-0.75}	5.3 ^{+0.4} _{-0.4}	9.11 ^{+3.17} _{-2.90}	9
J0935-0003	4.26	396 ± 35	370 ⁺⁰ ₋₉	3.30 ^{+0.35} _{-0.01}	13.21 ^{+0.00} _{-0.80}	4.1 ^{+0.0} _{-0.2}	0.02 ^{+1.08} _{-0.00}	9
J0936+0913	3.45	243 ± 11	243 ⁺¹¹ ₋₁₀	2.22 ^{+0.44} _{-0.42}	3.45 ^{+0.35} _{-0.30}	3.3 ^{+0.3} _{-0.3}	2.16 ^{+1.59} _{-1.42}	11
J0946+1006	4.95	263 ± 21	263 ⁺²⁰ ₋₂₀	3.77 ^{+0.78} _{-0.72}	4.92 ^{+0.90} _{-0.80}	5.6 ^{+1.0} _{-0.9}	6.12 ^{+3.34} _{-3.03}	10
J0956+5100	5.05	334 ± 15	334 ⁺¹⁵ ₋₁₄	3.23 ^{+0.51} _{-0.32}	8.44 ^{+0.90} _{-0.80}	5.6 ^{+0.6} _{-0.5}	1.34 ^{+2.11} _{-1.28}	9
J0959+4416	3.61	244 ± 19	243 ⁺¹⁹ ₋₁₈	2.78 ^{+0.95} _{-0.89}	3.81 ^{+0.75} _{-0.60}	3.3 ^{+0.6} _{-0.5}	3.74 ^{+3.60} _{-3.11}	11
J0959+0410	2.24	197 ± 13	197 ⁺¹² ₋₁₂	3.85 ^{+1.09} _{-0.89}	1.14 ^{+0.15} _{-0.15}	4.2 ^{+0.6} _{-0.6}	8.50 ^{+4.02} _{-3.21}	9
J1016+3859	3.13	247 ± 13	248 ⁺¹¹ ₋₁₃	3.29 ^{+0.84} _{-0.66}	2.54 ^{+0.25} _{-0.30}	4.0 ^{+0.4} _{-0.5}	4.96 ^{+3.20} _{-2.38}	9
J1020+1122	5.12	282 ± 18	282 ⁺¹⁸ ₋₁₇	4.45 ^{+0.71} _{-0.65}	5.06 ^{+0.75} _{-0.65}	3.8 ^{+0.6} _{-0.5}	7.18 ^{+3.11} _{-2.91}	9
J1023+4230	4.50	242 ± 15	243 ⁺¹⁴ ₋₁₅	4.01 ^{+0.58} _{-0.53}	3.06 ^{+0.40} _{-0.40}	3.8 ^{+0.5} _{-0.5}	7.51 ^{+2.47} _{-2.23}	10
J1029+0420	1.92	210 ± 9	210 ⁺⁷ ₋₇	1.94 ^{+0.63} _{-0.52}	1.29 ^{+0.10} _{-0.10}	3.5 ^{+0.3} _{-0.3}	2.31 ^{+2.07} _{-1.55}	9
J1100+5329	7.02	187 ± 23	187 ⁺²³ ₋₂₂	5.73 ^{+0.38} _{-0.48}	2.55 ^{+0.85} _{-0.65}	1.3 ^{+0.4} _{-0.3}	15.52 ^{+1.91} _{-2.41}	11
J1103+5322	2.78	196 ± 12	196 ⁺¹¹ ₋₁₂	2.95 ^{+0.75} _{-0.67}	2.32 ^{+0.30} _{-0.30}	3.4 ^{+0.4} _{-0.4}	5.91 ^{+2.73} _{-2.36}	12
J1106+5228	2.17	262 ± 9	262 ⁺³ ₋₆	1.85 ^{+0.41} _{-0.16}	1.80 ^{+0.05} _{-0.10}	3.4 ^{+0.1} _{-0.2}	0.52 ^{+1.24} _{-0.40}	7
J1112+0826	6.19	320 ± 20	320 ⁺¹⁹ ₋₁₈	4.31 ^{+0.44} _{-0.40}	5.75 ^{+0.80} _{-0.70}	4.5 ^{+0.6} _{-0.5}	4.66 ^{+2.35} _{-2.21}	8
J1134+6027	2.93	239 ± 11	239 ⁺⁹ ₋₁₀	2.63 ^{+0.59} _{-0.59}	2.77 ^{+0.25} _{-0.25}	4.4 ^{+0.4} _{-0.4}	3.45 ^{+2.14} _{-1.97}	10
J1142+1001	3.52	221 ± 22	222 ⁺²⁰ ₋₂₂	4.61 ^{+1.32} _{-1.06}	2.13 ^{+0.45} _{-0.45}	2.4 ^{+0.5} _{-0.5}	10.13 ^{+5.30} _{-4.22}	9
J1143-0144	3.27	269 ± 5	270 ⁺⁴ ₋₄	5.05 ^{+0.35} _{-0.26}	3.36 ^{+0.10} _{-0.10}	3.0 ^{+0.1} _{-0.1}	10.15 ^{+1.33} _{-1.02}	8
J1153+4612	3.18	226 ± 15	227 ⁺¹³ ₋₁₄	2.13 ^{+0.59} _{-0.44}	1.85 ^{+0.25} _{-0.25}	3.8 ^{+0.5} _{-0.5}	2.19 ^{+2.19} _{-1.54}	9
J1204+0358	3.68	267 ± 17	266 ⁺¹⁷ ₋₁₃	3.23 ^{+0.52} _{-0.61}	2.35 ^{+0.35} _{-0.25}	4.5 ^{+0.7} _{-0.5}	3.92 ^{+2.16} _{-2.44}	7
J1205+4910	4.27	281 ± 13	281 ⁺¹³ ₋₁₁	3.50 ^{+0.54} _{-0.55}	4.60 ^{+0.50} _{-0.40}	3.8 ^{+0.4} _{-0.3}	4.35 ^{+2.18} _{-2.18}	9
J1213+6708	3.13	292 ± 11	289 ⁺⁰ ₋₇	1.94 ^{+0.15} _{-0.00}	2.90 ^{+0.00} _{-0.15}	3.6 ^{+0.0} _{-0.2}	0.01 ^{+0.41} _{-0.00}	7
J1218+0830	3.47	219 ± 10	219 ⁺⁹ ₋₁₀	4.58 ^{+0.61} _{-0.52}	2.58 ^{+0.25} _{-0.25}	2.8 ^{+0.3} _{-0.3}	10.47 ^{+2.39} _{-2.04}	10
J1250+0523	4.18	252 ± 14	252 ⁺¹⁴ ₋₁₃	2.37 ^{+0.43} _{-0.36}	3.05 ^{+0.40} _{-0.35}	2.1 ^{+0.3} _{-0.2}	2.03 ^{+1.73} _{-1.41}	10
J1306+0600	3.87	237 ± 17	237 ⁺¹⁵ ₋₁₆	5.99 ^{+0.82} _{-0.82}	2.10 ^{+0.30} _{-0.30}	3.3 ^{+0.5} _{-0.5}	14.22 ^{+3.49} _{-3.42}	8
J1313+4615	4.25	263 ± 18	263 ⁺¹⁷ ₋₁₆	4.33 ^{+0.79} _{-0.76}	3.31 ^{+0.50} _{-0.45}	3.9 ^{+0.6} _{-0.5}	7.66 ^{+3.33} _{-3.16}	9
J1318-0313	6.01	213 ± 18	212 ⁺¹⁸ ₋₁₆	3.98 ^{+0.37} _{-0.44}	3.29 ^{+0.70} _{-0.55}	2.5 ^{+0.5} _{-0.4}	8.74 ^{+1.74} _{-2.04}	12
J1330-0148	1.32	185 ± 9	187 ⁺⁷ ₋₈	2.25 ^{+1.00} _{-0.63}	0.57 ^{+0.05} _{-0.05}	5.8 ^{+0.5} _{-0.5}	3.77 ^{+3.32} _{-1.99}	8
J1402+6321	4.53	267 ± 17	267 ⁺¹⁶ ₋₁₇	4.51 ^{+0.84} _{-0.74}	4.77 ^{+0.65} _{-0.65}	3.6 ^{+0.5} _{-0.5}	8.31 ^{+3.51} _{-3.03}	10
J1403+0006	2.62	213 ± 17	214 ⁺¹⁴ ₋₁₅	2.94 ^{+1.04} _{-0.85}	1.66 ^{+0.25} _{-0.25}	2.6 ^{+0.4} _{-0.4}	5.00 ^{+3.83} _{-2.97}	10

Strong lensing with superfluid dark matter

J1416+5136	6.08	240 ± 25	241 ⁺²⁴ ₋₂₃	4.91 ^{+0.49} _{-0.48}	2.61 ^{+0.60} _{-0.55}	2.5 ^{+0.6} _{-0.5}	10.24 ^{+2.66} _{-2.64}	9
J1420+6019	1.26	205 ± 4	203 ⁺⁴ ₋₀	1.73 ^{+0.00} _{-0.27}	1.05 ^{+0.05} _{-0.00}	3.2 ^{+0.2} _{-0.0}	2.05 ^{+0.00} _{-0.82}	8
J1430+4105	6.53	322 ± 32	322 ⁺³² ₋₃₂	4.43 ^{+1.01} _{-0.81}	9.63 ^{+2.30} _{-2.00}	5.3 ^{+1.3} _{-1.1}	5.58 ^{+4.85} _{-4.02}	10
J1436-0000	4.80	224 ± 17	224 ⁺¹⁷ ₋₁₅	3.49 ^{+0.49} _{-0.55}	3.08 ^{+0.55} _{-0.45}	2.1 ^{+0.4} _{-0.3}	6.53 ^{+2.11} _{-2.32}	11
J1443+0304	1.93	209 ± 11	208 ⁺¹¹ ₋₆	2.96 ^{+0.49} _{-0.83}	0.85 ^{+0.10} _{-0.05}	3.0 ^{+0.4} _{-0.2}	5.15 ^{+1.73} _{-2.82}	7
J1451-0239	2.33	223 ± 14	222 ⁺¹⁴ ₋₁₂	2.28 ^{+0.97} _{-0.84}	1.67 ^{+0.25} _{-0.20}	2.5 ^{+0.4} _{-0.3}	2.89 ^{+3.35} _{-2.58}	9
J1525+3327	6.55	264 ± 26	264 ⁺²⁵ ₋₂₆	4.87 ^{+0.80} _{-0.73}	6.67 ^{+1.55} _{-1.45}	2.5 ^{+0.6} _{-0.5}	9.76 ^{+3.81} _{-3.48}	11
J1531-0105	4.71	279 ± 12	278 ⁺¹² ₋₁₀	3.74 ^{+0.37} _{-0.40}	3.95 ^{+0.40} _{-0.30}	3.1 ^{+0.3} _{-0.2}	5.28 ^{+1.59} _{-1.75}	8
J1538+5817	2.50	189 ± 12	189 ⁺⁹ ₋₉	5.20 ^{+0.72} _{-0.69}	0.95 ^{+0.10} _{-0.10}	2.2 ^{+0.2} _{-0.2}	13.20 ^{+2.77} _{-2.62}	9
J1614+4522	2.54	182 ± 13	182 ⁺¹² ₋₁₃	2.43 ^{+0.80} _{-0.70}	1.94 ^{+0.30} _{-0.30}	3.0 ^{+0.5} _{-0.5}	4.67 ^{+2.84} _{-2.35}	13
J1621+3931	4.97	236 ± 20	237 ⁺¹⁸ ₋₂₀	5.12 ^{+0.77} _{-0.67}	3.05 ^{+0.55} _{-0.55}	2.2 ^{+0.4} _{-0.4}	11.32 ^{+3.41} _{-2.97}	10
J1627-0053	4.18	290 ± 14	290 ⁺¹² ₋₁₃	2.38 ^{+0.44} _{-0.27}	5.19 ^{+0.55} _{-0.50}	5.2 ^{+0.6} _{-0.5}	0.93 ^{+1.65} _{-0.92}	9
J1630+4520	6.91	276 ± 16	276 ⁺¹⁶ ₋₁₅	4.80 ^{+0.31} _{-0.32}	4.58 ^{+0.60} _{-0.55}	3.3 ^{+0.4} _{-0.4}	8.63 ^{+1.75} _{-1.78}	9
J1636+4707	3.96	231 ± 15	231 ⁺¹⁵ ₋₁₄	3.02 ^{+0.64} _{-0.57}	2.94 ^{+0.45} _{-0.40}	3.1 ^{+0.5} _{-0.4}	4.83 ^{+2.53} _{-2.23}	11
J1644+2625	3.07	229 ± 12	230 ⁺¹⁰ ₋₁₁	3.77 ^{+0.68} _{-0.68}	1.94 ^{+0.20} _{-0.20}	3.2 ^{+0.3} _{-0.3}	7.20 ^{+2.62} _{-2.52}	9
J1719+2939	3.89	286 ± 15	286 ⁺¹⁰ ₋₁₄	2.28 ^{+0.49} _{-0.19}	3.70 ^{+0.30} _{-0.40}	5.8 ^{+0.5} _{-0.6}	0.63 ^{+1.82} _{-0.62}	8
J2238-0754	3.08	198 ± 11	198 ⁺¹¹ ₋₉	5.07 ^{+0.57} _{-0.69}	1.56 ^{+0.20} _{-0.15}	2.3 ^{+0.3} _{-0.2}	12.68 ^{+2.23} _{-2.68}	10
J2300+0022	4.51	279 ± 17	279 ⁺¹⁶ ₋₁₆	4.83 ^{+0.73} _{-0.77}	4.22 ^{+0.55} _{-0.50}	4.5 ^{+0.6} _{-0.5}	8.49 ^{+3.16} _{-3.22}	9
J2303+1422	4.35	255 ± 16	255 ⁺¹⁶ ₋₁₆	5.00 ^{+0.83} _{-0.80}	4.23 ^{+0.60} _{-0.55}	3.4 ^{+0.5} _{-0.4}	10.62 ^{+3.42} _{-3.27}	9
J2321-0939	2.47	249 ± 8	250 ⁺⁷ ₋₇	3.82 ^{+0.63} _{-0.72}	3.18 ^{+0.20} _{-0.20}	3.7 ^{+0.2} _{-0.2}	7.16 ^{+2.31} _{-2.51}	9
J2341+0000	4.50	207 ± 13	207 ⁺¹² ₋₁₃	4.80 ^{+0.50} _{-0.48}	2.59 ^{+0.35} _{-0.35}	2.3 ^{+0.3} _{-0.3}	11.56 ^{+2.13} _{-2.01}	11
J2347-0005	6.10	404 ± 59	368 ⁺⁰ ₋₂₃	3.56 ^{+0.27} _{-0.00}	9.13 ^{+0.00} _{-1.25}	4.4 ^{+0.0} _{-0.6}	0.01 ^{+1.63} _{-0.00}	8